This document is published in:

International Journal of Solids and Structures, 2013, 50, 2, 339-351.
Doi: http://dx.doi.org/10.1016/j.ijsolstr.2012.09.019.

Experimental and numerical analysis of the martensitic transformation in AISI 304 steel sheets subjected to perforation by conical and hemispherical projectiles

J.A. Rodríguez-Martínez [a], A. Rusinek [b], R. Pesci [c], R. Zaera [a,*]

[a] Department of Continuum Mechanics and Structural Analysis, University Carlos III of Madrid, Avda. de la Universidad, 30, 28911 Leganés, Madrid, Spain
[b] Laboratory of Mechanics, Biomechanics, Polymers and Structures (LaBPS), National Engineering School of Metz (ENIM), Route d'Ars Laquenexy, CS65820 57078 Metz Cedex 3, France
[c] ENSAM-Arts et Métiers ParisTech, Laboratoire d'Etudes des Microstructures et de Mécanique des Matériaux LEM3, UMR CNRS 7239, 4 Rue Augustin Fresnel, 57078 Metz Cedex 3, France

Keywords:
Perforation
Martensitic transformation
AISI 304
Dynamic failure
Numerical simulations

A B S T R A C T

In this work, an experimental and numerical analysis of the martensitic transformation in AISI 304 steel sheets subjected to perforation by conical and hemispherical projectiles is conducted. Experiments are performed using a pneumatic gas gun for with the impact velocities in the range of $35\ \mathrm{m/s} < V_0 < 200\ \mathrm{m/s}$. Two target thicknesses are examined, $t_1 = 0.5$ mm and $t_2 = 1.0$ mm. The experimental setup enabled the determination of the impact velocity, the residual velocity and the failure mode of the steel sheets. The effect of the projectile nose shape on the target's capacity for energy absorption is evaluated. Moreover, martensite is detected in all the impacted samples, and the role played by the projectile nose shape on the transformation is highlighted. A three-dimensional model is developed in ABAQUS/Explicit to simulate the perforation tests. The material is defined via the constitutive model developed by Zaera et al. (2012) to describe the strain-induced martensitic transformation occurring in metastable austenitic steels at high strain rates. The finite element results are compared with the experimental evidence, and satisfactory matching is observed over the entire range of impact velocities tested and for both projectile configurations and target thicknesses considered. The numerical model succeeds in describing the perforation mechanisms associated with each projectile-target configuration analyzed. The roles played by impact velocity, target thickness and projectile nose shape on the martensitic transformation are properly captured.

1. Introduction

Steel sheet is a cost-effective and easily affordable material, with valuable properties for industry. In some industrial applications, they are prone to suffer dynamic indentation or perforation: high-speed blanking and hole flanging in manufacturing processes, or impact with objects in vehicles, vessels, marine hulls and shields. Thus, the deformation and the damage initiation/development in the target are relevant phenomena which should be considered when assessing the performance of steel sheets against impact loading. Since the pioneering work of Goldsmith et al. (Goldsmith and Finnegan, 1971; Calder and Goldsmith, 1971; Backman and Goldsmith, 1978); Corran et al. (1983) or Leppin and Woodward (1986) several papers have been published on the perforation of thin plates by blunt, conical or hemispherical projectiles (Corbett et al., 1996; Wierzbicki, 1999; Børvik et al., 1999; Børvik et al., 2002a,b; Rodríguez-Martínez et al., 2010a,b,c, 2011b; Jones and Paik, 2012).

The perforation of sheets by hemispherical strikers produces a circumferential neck, followed by circumferential cracking (discing). As the impact velocity increases, a hinged cap forms in the sheet and remains attached. Higher impact velocities produce a clean separation and ejection of the cap and short radial cracks. Conical shapes cause failure through radial cracking and tearing out into a number of petals. Energy absorption is then driven by a combination of processes: bending and stretching of the plate (structural response), fracture and petal curling (local response).

Most of the works cited in the previous paragraphs address aluminum, mild steel, copper or brass. Only a few of them (Dean et al., 2009; Rodríguez-Martínez et al., 2010c) have considered metastable austenitic steel alloys exhibiting *Strain-Induced Martensitic Transformation* (SIMT). These grades have the ability to transform from the initial face-centered cubic austenite phase γ to body-centered cubic martensite α' during plastic deformation. The hardness of martensite is usually higher than that of the austenite, increasing the yield stress and the strain hardening of the two-phase steel. Additionally, the martensitic transformation causes the TRansformation Induced Plasticity (TRIP) effect, and therefore, steels showing SIMT are usually known as TRIP steels (Iwamoto et al.,

* Corresponding author. Tel.: +34 916249983; fax: +34 916249430.
E-mail address: ramon.zaera@uc3m.es (R. Zaera).

http://dx.doi.org/10.1016/j.ijsolstr.2012.09.019

1998). TRIP enhances the work hardenability of the steel, delays the onset of necking, and thus improves formability (Lichtenfeld et al., 2006; Dan et al., 2008; Oliver et al., 2007). Because of their ductility and work hardening property, metastable austenitic alloys exhibiting SIMT are commonly used for energy absorption in impact and blast applications (Andersson, 2005; Langdon and Schleyer, 2005a,b, 2006).

This work presents an experimental and numerical analysis of the martensitic transformation in AISI 304 steel sheets subjected to perforation by conical and hemispherical projectiles. Perforation tests are carried out using a pneumatic gas gun for impact velocities in the range of $35\ \mathrm{m/s} < V_0 < 200\ \mathrm{m/s}$. The experimental arrangement enables the determination of the impact velocity, the residual velocity and the failure mode of the steel sheets. It has been determined that the SIMT occurs during perforation for all the tests performed. Moreover, a three-dimensional model is developed in ABAQUS/Explicit to simulate the perforation tests. The material is described by the constitutive model developed by Zaera et al. (2012). The finite element results are correlated with the experimental evidence and satisfactory agreement is found for all the projectile-target configurations examined. The roles played by impact velocity, target thickness and projectile nose shape on the martensitic transformation are properly captured.

2. The AISI 304 steel

The material studied in this work is the AISI 304 austenitic stainless steel. The austenitic group (in the undeformed state, the austenitic steels are composed of 100% austenite) contains more grades that are used in greater quantities than any other category of stainless steel. Austenitic stainless steels exhibit corrosion resistance superior to both ferritic and martensitic stainless steels. In addition, they offer excellent formability.

Among the austenitic stainless steel grades, AISI 304 is the most versatile and the most widely used. It serves in a wide range of applications because of its strength, work hardening, ductility and excellent formability. Thus, its use has been fostered in a number of applications including the transportation sector, the petrochemical and the nuclear industries and various types of construction.

The chemical composition of the material is given in Table 1. Over the last decade, AISI 304 has raised the interest of researchers because of its ability to transform from the initial face-centered cubic austenite phase γ to body-centered cubic martensite α' under wide ranges of loading conditions (Iwamoto et al., 1998; De et al., 2006; Hecker et al., 1982; Mertinger et al., 2008; Tomita and Iwamoto, 1995; Tomita and Iwamoto, 2001; Rodríguez-Martínez et al., 2011a; Zaera et al., 2012). A detailed experimental analysis concerning the dependence of the material flow stress on strain, strain rate and temperature can be found elsewhere (Angel, 1954; Huang et al., 1989; Rodríguez-Martínez et al., 2011a). Especially remarkable is the fact that, for this material, the phase transformation is observable during high-rate loading events (Rodríguez-Martínez et al., 2010c). This transformation during rapid straining processes characterizes the mechanical response of AISI 304 steel under dynamic loading.

3. Testing stand for perforation of steel sheets

A drawing of the samples used in the perforation tests is shown in Fig. 1. The tested square sheets were $A_0 = 130 \times 130\ \mathrm{mm}^2$ and their active surface area, after they were screwed and clamped to the support, was $A_f = 100 \times 100\ \mathrm{mm}^2$. Two different target thicknesses have been considered, $t_1 = 0.5$ mm and $t_2 = 1.0$ mm.

Table 1
Chemical composition of AISI 304 steel (wt.%).

C	Mn	Cr	Ni	Mo	Cu	Si	Nb
0.06	1.54	18.47	8.30	0.30	0.37	0.48	0.03

Hemispherical and conical projectiles were used in the perforation tests. The masses of both projectile types were $M_p = 30$ g; their geometries and dimensions are shown in Fig. 2. The projectiles were fabricated using Maraging steel, which exhibits a higher yield stress – $\sigma_y \approx 2000$ MPa – than that of AISI 304 steel under dynamic conditions of deformation. In addition, the projectiles underwent a heat treatment to increase their hardness.

To perform perpendicular impact tests on the steel sheets, a pneumatic gas gun was used, see Fig. 3. It should be noted that the diameter of the barrel was roughly equal to the diameter of the projectiles. No sabot was required for guidance of the projectile inside the barrel, which helps to ensure the perpendicularity of the impact.

The initial impact velocity, V_0, and the residual impact velocity, V_r, were measured using lasers coupled to photodiodes and time counters, see references D and F in Fig. 3. When the projectile passes through the laser beam, a time counter is triggered. This procedure is repeated twice (twice before the impact and twice after), defining the time interval. Then, the impact velocity $V_0 = \Delta X_{12}^{laser}/\Delta t_{12}$, and the residual velocity $V_r = \Delta X_{34}^{laser}/\Delta t_{34}$ are determined, where ΔX_{ij}^{laser} is the predetermined distance between the lasers i and j and Δt_{ij} is the recorded time interval for the lasers i and j. Next, the experimental results are discussed.

4. Experimental results

Perforation experiments were performed using both projectile types presented in the previous section for both target thicknesses t_1 and t_2 with impact velocities in the range of $35\ \mathrm{m/s} < V_0 < 200\ \mathrm{m/s}$. It should be noted that, for all the tests performed, the projectile showed an absence of plastic straining, damage or erosion after the impact.

In Fig. 4, the experimental results obtained using the conical projectile configuration are depicted as residual velocity versus impact velocity (V_r–V_0) curves. For the target thickness $t_1 = 0.5$ mm, the ballistic limit was found to be $V_{bl} \approx 38$ m/s. Because of the small thickness of the target, once the ballistic limit velocity is exceeded, i.e., $V_0 > V_{bl}$, the V_r–V_0 curve rapidly approaches the condition determined by $V_r = V_0$. For the target thickness $t_2 = 1.0$ mm, the ballistic limit was found to be $V_{bl} \approx 75$ m/s, which is nearly double than that determined for the target thickness t_1. Close to the ballistic limit condition, a rather small increase in the impact velocity leads to a quite rapid rise in the residual velocity. In comparison to the target thickness configuration $t_1 = 0.5$ mm and within the range of impact velocities tested, the greater capability for energy absorption of the target in the case of $t_2 = 1.0$ mm becomes evident.

The results shown in Fig. 4 have been fitted via the expression proposed by Recht and Ipson (1963),

$$V_r = \left(V_0^{\kappa} - V_{bl}^{\kappa}\right)^{1/\kappa} \tag{1}$$

where κ is a fitting parameter. The values of κ determined were $\kappa = 1.79$ for $t_1 = 0.5$ mm and $\kappa = 1.90$ for $t_2 = 1.0$ mm.

Moreover, it was observed that petalling is the final stage of the perforation process for all the tests performed using the conical projectile configuration, as shown in Fig. 5. The number of petals varied between three and five for all cases. It should be noted that this number of petals is frequently reported in the literature (Atkins et al., 1998; Rodríguez-Martínez et al., 2010a, 2011b) for boundary value problems involving perforation of metallic sheets by conical projectiles at low/intermediate impact velocities. In successive publications Wierzbicki (1999) and Lee and Wierzbicki

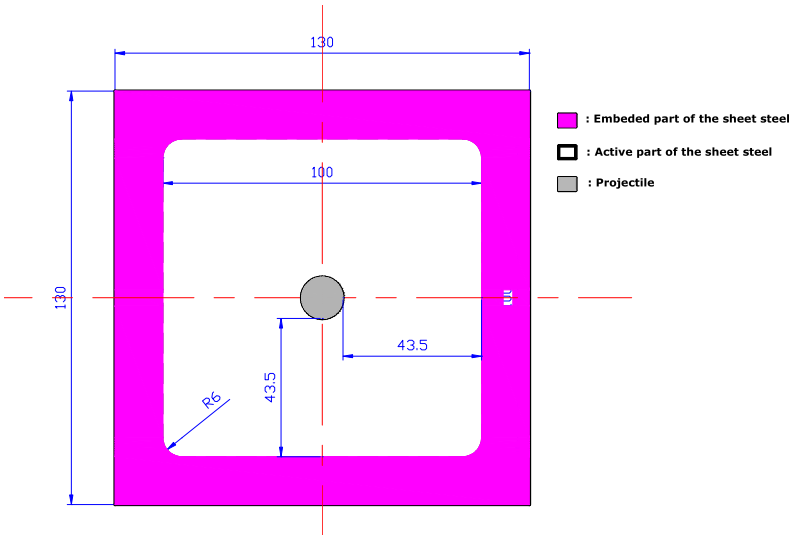

Fig. 1. Geometry and dimensions (mm) of the samples used in the experiments.

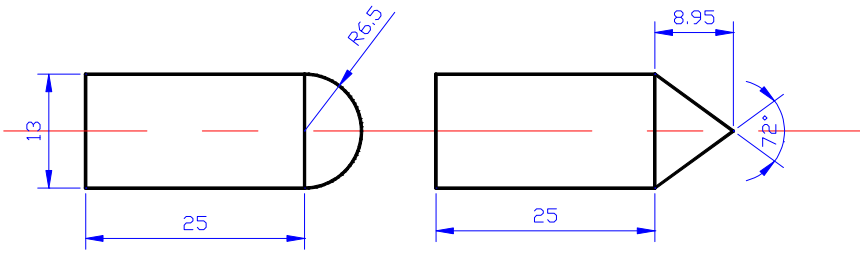

Fig. 2. Geometry and dimensions (mm) of the projectiles used in the experiments.

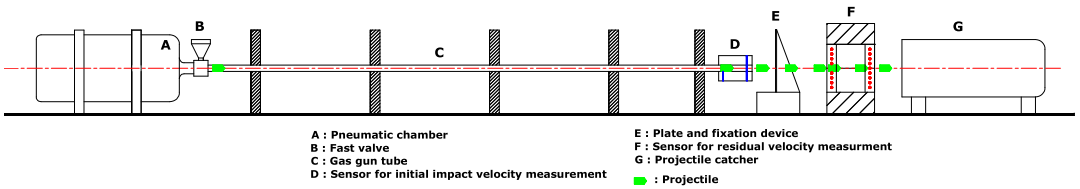

Fig. 3. Description of the experimental setup.

(2005) explained this recurring number of petals based on theoretical considerations that correlate the formation of three to five petals to a minimum of the total rate of energy dissipation.

The next step is to determine if the martensitic transformation occurs in the steel sheets during perforation. For that task, the impacted plates were cut and the petals and the cracking interfaces were examined using a Scanning Electron Microscope (SEM). For the entire range of impact velocities covered, martensite was found in the tested specimens, as can be observed in Fig. 6. Numerous grains that were partially transformed for different variants were detected. However, the complicated shape of the tested samples in the zone directly affected by the impact made the application of X-ray diffraction technique difficult for determining the volume fraction of martensite. The formation of martensite in AISI 304 steels sheets subjected to perforation by conical projectiles was previously detected by Rodríguez-Martínez et al. (2010c); however, in the present work, the range of impact velocities tested is considerably larger. Thus, this work provides further corroboration

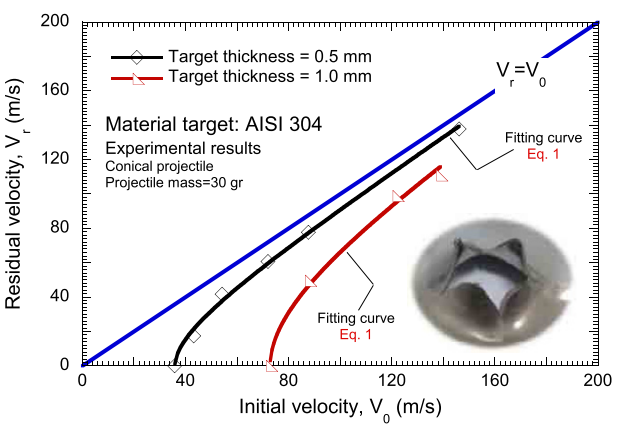

Fig. 4. Experimental results: conical projectile configuration. Residual velocity V_r versus initial velocity V_0 for both target thicknesses analyzed, $t_1 = 0.5$ mm and $t_2 = 1.0$ mm.

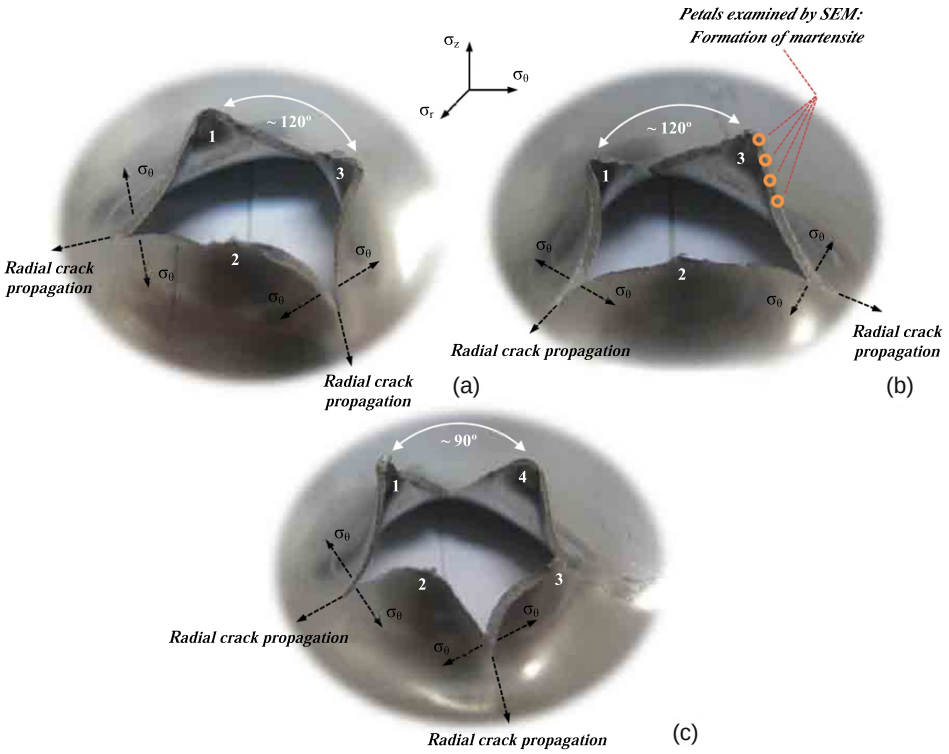

Fig. 5. Experimental results: conical projectile configuration. Final stage of the impact process for different initial velocities. Target thickness $t_2 = 1$ mm. (a) $V_0 = 86.21$ m/s, (b) $V_0 = 136.01$ m/s, (c) $V_0 = 176.06$ m/s.

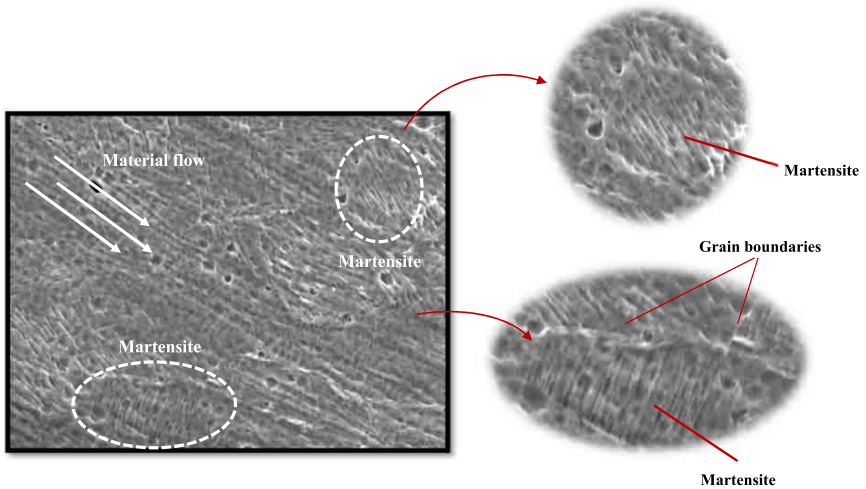

Fig. 6. Conical projectile configuration. SEM micrograph of the zone directly affected by the impact. Target thickness $t_2 = 1.0$ mm. Impact velocity $V_0 = 136.01$ m/s.

of the ability of this material to undergo the γ to α' transformation under high loading rate events associated with a strong adiabatic temperature increase.

In Fig. 7, the experimental results for the hemispherical projectile configuration are illustrated via V_r—V_0 curves. For the target thickness $t_1 = 0.5$ mm the ballistic limit was $V_{bl} \approx 95$ m/s and for $t_2 = 1.0$ mm the limit was $V_{bl} \approx 130$ m/s. The results shown in Fig. 7 have been fitted using Eq. (1). The values of κ determined were $\kappa = 2.17$ for $t_1 = 0.5$ mm and $\kappa = 2.19$ for $t_2 = 1.0$ mm.

In comparison with the conical projectile configuration, the ballistic limit is considerably higher, which means the hemispherical projectile is less efficient than the conical one for perforating the steel targets (Børvik et al., 2002a). Over the range of impact velocities tested and for both target thicknesses examined, the V_r—V_0 curves remain far from the condition determined by $V_r = V_0$. The ability of the target to dissipate energy in the form of plastic deformation is larger when the hemispherical projectiles are used. This is illustrated in Fig. 8, where the final stage of the impact process is

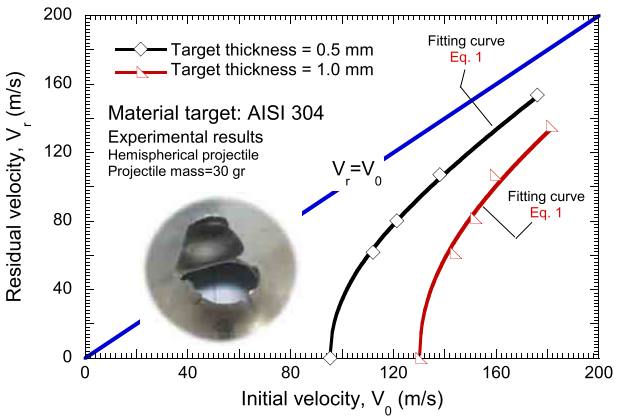

Fig. 7. Experimental results: hemispherical projectile configuration. Residual velocity V_r versus initial velocity V_0 for both target thicknesses tested, $t_1 = 0.5$ mm and $t_2 = 1.0$ mm.

shown for different initial velocities. For the hemispherical projectile configuration, substantial bending of the steel sheets during perforation leads to considerable radial sliding of the projectile over the plate. Consequently, an extended target zone subjected to severe plastic deformation is observed. Necking formation and the subsequent propagation of radial cracks is the recurrent failure mode of the plates, as can be observed in Fig. 8. Necking takes place close to the dome of the projectile/plate contact area. A plug ejection occurs if the impact velocity is sufficiently high. The plug size and number of radial cracks formed increased with increasing impact velocity.

The target zones surrounding the necking and the ejected plugs were examined using a SEM. For the complete range of impact velocities covered, martensite was found in the test specimens, as can be observed in Fig. 9. It was concluded that the amount of martensite observed is larger than that found in the plates impacted by conical projectiles. In addition, the extent of the target in which martensite was detected was larger than that determined for the conical projectile configuration. This fact becomes evident if one bears in mind that the target zone subjected to severe plastic deformation is larger when the hemispherical projectiles are used.

Next, a summary of the three-dimensional constitutive model developed by Zaera et al. (2012) to describe the SIMT taking place in metastable austenitic steels deforming at high strain rates is introduced.

5. A three-dimensional constitutive model for metastable austenitic steels

The constitutive description is based on the previous works of Olson and Cohen (1975); Stringfellow et al. (1992) and Papatriantafillou et al. (2004), all developed to account for SIMT in steels containing metastable austenite, and includes modifications in the following items:

- According to Olson and Cohen (1975), the intersection of the shear bands in austenite is considered as the dominant mechanism of SIMT. The kinetics of the transformation is described by an exponential expression in which the plastic deformation in austenite is multiplied by a coefficient α favoring the shear band deformation mode. The dependence of α on the temperature has been defined in the model through an exponential law that captures the decrease of the transformation rate with increasing temperature within the SIMT temperature range.
- The linearly temperature-dependent normalized thermodynamic driving force for the martensitic transformation, proposed by Stringfellow et al. (1992), is replaced here by an exponential equation. This new law provides a greater temperature sensitivity of the rate of martensitic transformation. This becomes relevant at high strain rates, where the temperature rise of the material results from the adiabatic character of the plastic deformation. According to the experimental results reported by Rodríguez-Martínez et al. (2011a), at high deformation rates, and therefore for significant temperature increases, small temperature variations lead to significant differences in the volume fraction of martensite formed.
- The thermal deformation tensor rate is included in the generalized Hooke's law for hypoelastic–plastic materials, taking into account that the adiabatic increase in temperature may lead to non-negligible thermal strains.

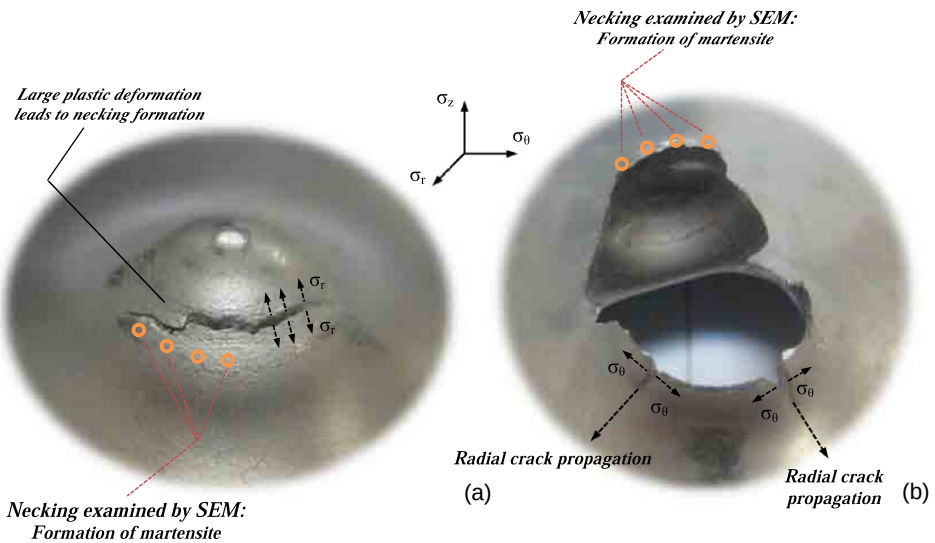

Fig. 8. Experimental results: hemispherical projectile configuration. Final stage of the impact process for different initial velocities. Target thickness $t_2 = 1$ mm. (a) $V_0 = 138.12$ m/s, (b) $V_0 = 163.20$ m/s.

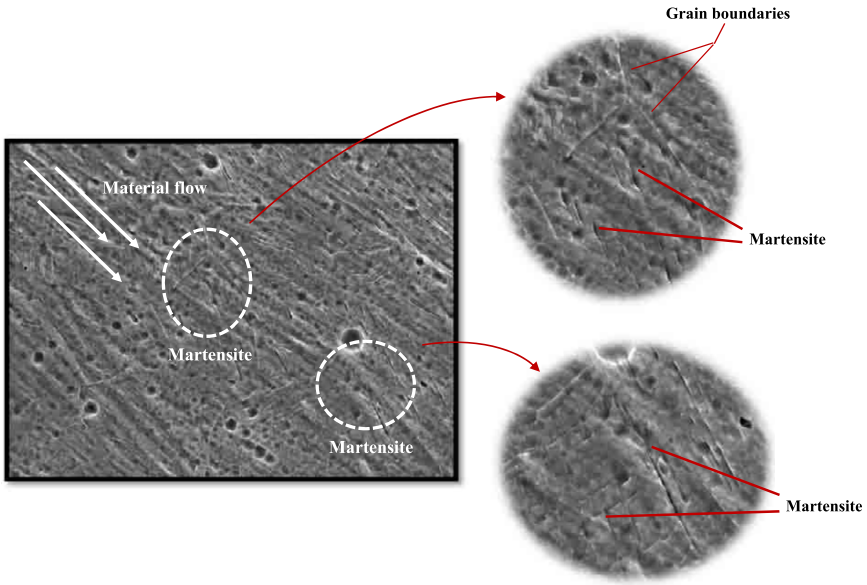

Fig. 9. Hemispherical projectile configuration. SEM micrograph of the zone directly affected by the impact. Target thickness $t_1 = 0.5$ mm. Impact velocity $V_0 = 112.10$ m/s.

- The effective properties of the thermo-viscoplastic heterogeneous material are calculated using a plastic potential, including viscous and thermal effects for both austenite and martensite, using the modified secant method proposed by Suquet (1995a), Suquet (1995b) and Suquet (1996) and the solution algorithm developed by Papatriantafillou et al. (2004).

An explicit scheme has been adopted to integrate the above equations. In a previous work (Zaera et al., 2012), the differential equations were discretized following a fully implicit algorithm. Nevertheless, because of the small time step characteristic of explicit codes, no difference was found in the results of the simulations using forward or backward integration. In addition, the explicit scheme used to integrate the constitutive model permitted a significant reduction in the computational time.

The constitutive model has been validated with experimental results of dynamic tensile tests at $\dot{\varepsilon} = 10, 100$ and $500\ s^{-1}$ on AISI 304 sheet steel specimens, and the model predictions correlate well with the experimental evidence in terms of macroscopic stress–strain curves and martensite volume fraction formed at high strain rates. Fig. 10 shows an example of the validation curves corresponding to $\dot{\varepsilon} = 100\ s^{-1}$. A complete description of the model and the values of the parameters identified for AISI 304 stainless steel can be found in Zaera et al. (2012).

The sheet targets for the impact tests and the sheet specimens used to characterize (Rodríguez-Martínez et al., 2011a) and model (Zaera et al., 2012) the material behavior were machined from the same plates.

6. Finite element configuration

A Lagrangian 3D finite element model for the simulation of the perforation process of the AISI 304 steel sheets was developed in ABAQUS/Explicit (HKS, 2010). A fully 3D configuration allows the model to describe the radial cracking and the petalling failure mode that characterize the perforation of metallic sheets by conical and hemispherical projectiles (Rusinek et al., 2009).

The target mesh developed is shown in Fig. 11. Four elements were placed across the thickness of the target. This is in agreement with the recommendations reported elsewhere (HKS, 2010), where

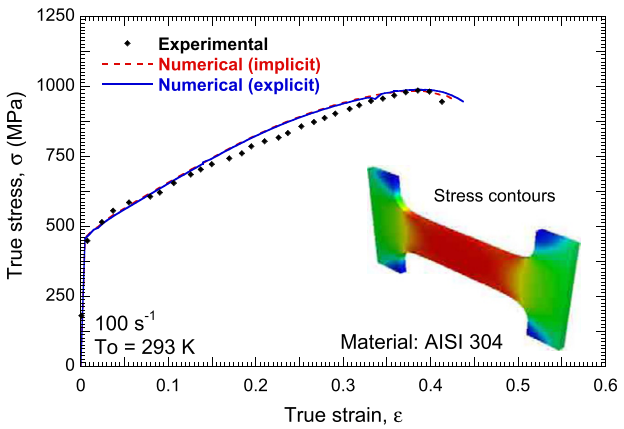

Fig. 10. Stress–strain curve in dynamic tensile test at $\theta_0 = 293$ K and $\dot{\varepsilon} = 100\ s^{-1}$. Comparison between experimental results (Rodríguez-Martínez et al., 2011a) and numerical results using implicit (Zaera et al., 2012) or explicit schemes for the integration of the constitutive model.

it is suggested that at least four elements should be used through the thickness when modeling any structures carrying bending loads. The mesh is split into three different zones:

- Zone I – This zone shows an unstructured mesh defined by 13720 tetrahedral elements, *C3D4* in ABAQUS notation (HKS, 2010). The initial strain localization is achieved in the simulations by numerical perturbations of the unstructured mesh. The flow localization pattern observed in the simulations was found to be practically insensitive to the initial numerical perturbation (i.e., to the mesh).
- Zone II – This zone shows radial symmetry. Thus, crack propagation does not show spurious directions artificially caused by inappropriate element alignments. Region II was meshed with 12800 8-node tri-linear elements with reduced integration, *C3D8R* in ABAQUS notation (HKS, 2010). The viscous approach available in ABAQUS/Explicit was used to prevent hourglass deformation modes; the scale factor used for all hourglass stiffnesses was set equal to one.

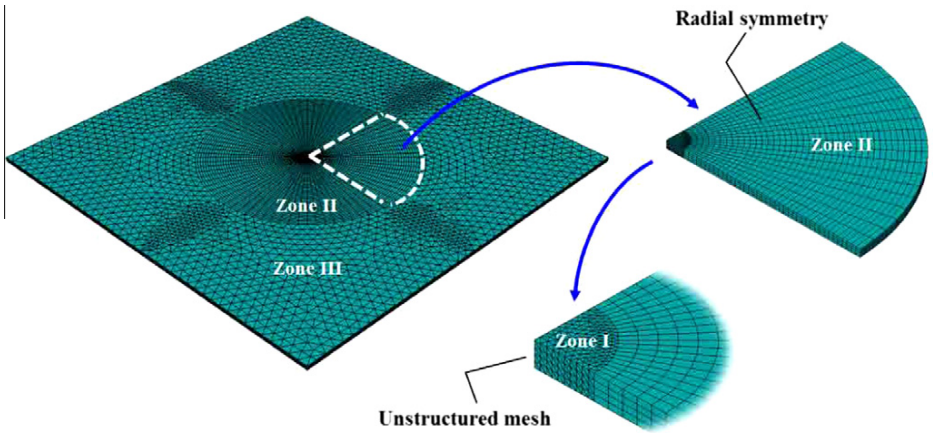

Fig. 11. Target mesh used in the numerical simulations.

- Zone III – This zone shows an unstructured mesh defined by 15,542 tetrahedral elements. Region III is located sufficiently far from the zone directly affected by the impact to not show a noticeable influence on the numerical results.

This mesh configuration was derived from a sensitivity analysis. It provides results in terms of energy absorbed by the target and martensite formation (practically) independent of the mesh density. This will be illustrated in forthcoming sections of the paper. Mesh-independent results are enhanced by the viscoplastic approach considered to define the material behavior. It has been demonstrated that viscoplasticity acts as a natural regularization method for solving mesh-dependent strain softening problems of plasticity (Glema et al., 2000; Voyiadjis and Abed, 2006). This approach creates a well-posed boundary value problem (Nemes and Eftis, 1993).

Based on the experimental evidence, which revealed the absence of erosion on the projectile-surface after impact, the projectile was defined as a rigid body. This assumption reduces the computational time required for the simulations. A constant value of 0.1 of the Coulomb friction coefficient μ was used to define the contact between the projectile and the plate, as was used by several other authors (Børvik et al., 1999, 2002b; Gupta et al., 2006, 2007; Arias et al., 2008; Rodríguez-Martínez et al., 2010b). The potential dependence of the friction coefficient on the temperature and the sliding velocity is not taken into account. The constant value used for the friction coefficient is based on the assumption of a constant pressure along the projectile-plate contact zone. The authors confirmed this hypothesis by FE analysis of different projectile-target configurations (Rusinek et al., 2009; Rodríguez-Martínez et al., 2010b). In any case, it has to be emphasized that the applicability of this simplification is restricted to metallic targets of small thicknesses, and further investigations would be required to describe accurately the interaction between the projectile and the plate.

To simulate the perforation process within a Lagrangian framework, a failure criterion must be considered. The use of failure criteria founded on the material deformation behavior is a practice widely accepted in the analysis of metallic structures subjected to dynamic loads (Johnson and Cook, 1985; Bao and Wierzbicki, 2004). In this work, the material failure is defined by a constant value of the equivalent plastic strain (Wood, 1965; Teng and Wierzbicki, 2006; Zhang and Ravi-Chandar, 2008). It must be noted that this simplified estimation of the failure strain produces numerical results in agreement with experiments (as will be shown later) because of the particularities of the boundary value problem approach. Since the target is very thin, the stress field across the thickness of the plate is nearly constant during the perforation process (as mentioned previously, the pressure along the projectile-plate contact is constant). The failure of the target, because of the ductile hole enlargement and the subsequent necking as reported in Section 4, involves stress triaxiality values of $\Sigma \geqslant 1/2$, (Rodríguez-Martínez et al., 2010b). For ductile metals within that range of stress states, the failure strain usually

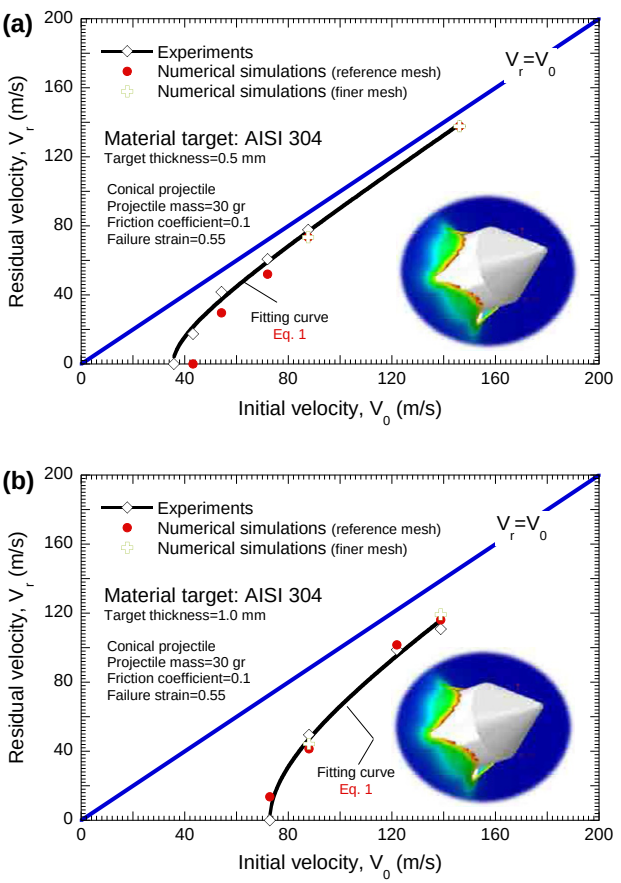

Fig. 12. Conical projectile configuration. Residual velocity V_r versus initial velocity V_0. Comparison between experiments and numerical simulations. (a) Target thickness $t_1 = 0.5$ mm, (b) target thickness $t_2 = 1.0$ mm.

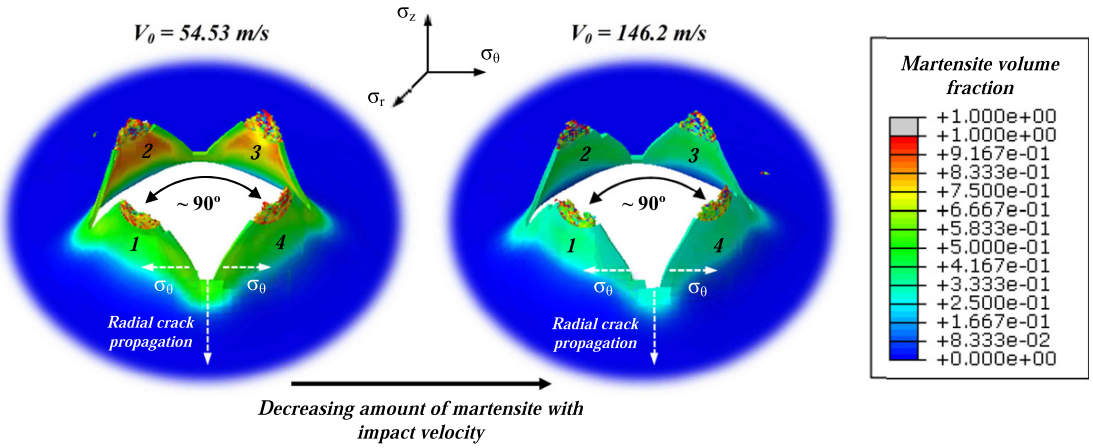

Fig. 13. Conical projectile configuration. Final stage of the perforation process for different impact velocities. Volume fraction of martensite contours. Target thickness $t_1 = 0.5$ mm.

becomes largely independent of triaxiality, as reported elsewhere (Dey et al., 2004).

The value of the failure strain adopted in the simulations, $\varepsilon_f^p = 0.55$, was estimated from the experimental observations of the material deformation behavior. This value is slightly higher than that corresponding to the necking strain under dynamic loading (Rodríguez-Martínez et al., 2011a). This adequately defines in the FE simulations the process of strain localization and necking formation that leads to the target collapse. In any case, the authors assume that further investigations concerning the dependence of the failure strain on the stress state, the strain rate and the temperature should be conducted for AISI 304 steel.

It is important to note that the failure criterion applied involves element deletion. Therefore, special attention has to be paid to the energy balance and its preservation during numerical simulations. It should be noted that the number of elements deleted during the FE analysis was very small. The elimination of elements was restricted to the crack propagation stage, and therefore, the mass conservation was assumed to be preserved.

7. Validation and discussion of the finite element results

7.1. Conical projectile configuration

The FE results for the conical projectile configuration are analyzed in the following. Fig. 12 shows the comparison between the experimental results and the numerical simulations in terms of V_r—V_0 curves for both target thicknesses examined. The numerical results obtained using both the reference mesh configuration (4 elements across the thickness) and a finer mesh (5 elements across the thickness) are shown. In both cases, the numerical results are practically identical, and the agreement with experiments is rather satisfactory. The difference is less than 15% over the entire range of impact velocities considered. The mesh-independent numerical results allow the use of the reference mesh configuration with 4 elements across the thickness of the target in the conical projectile simulations.

The model properly predicts the characteristic failure mode of the plates. Petalling formation occurs at the final stage of the perforation process over the entire range of impact velocities examined. The number of petals varies between four and six, close to the experimental evidence. The former represents the case of impact velocities close to the ballistic limit, and the latter, the case of the highest impact velocities tested. The number of petals also varies with the target thickness. Furthermore, the location of petals depends on both, the impact velocity and the target thickness. This reinforces the idea that the numerical perturbations coming from the unstructured mesh and the round-off errors throughout the integration process are sufficient to trigger instability in problems having geometrical and loading symmetries. A similar approach (no artificial imperfections) was successfully applied by the authors to other problems having geometrical and loading

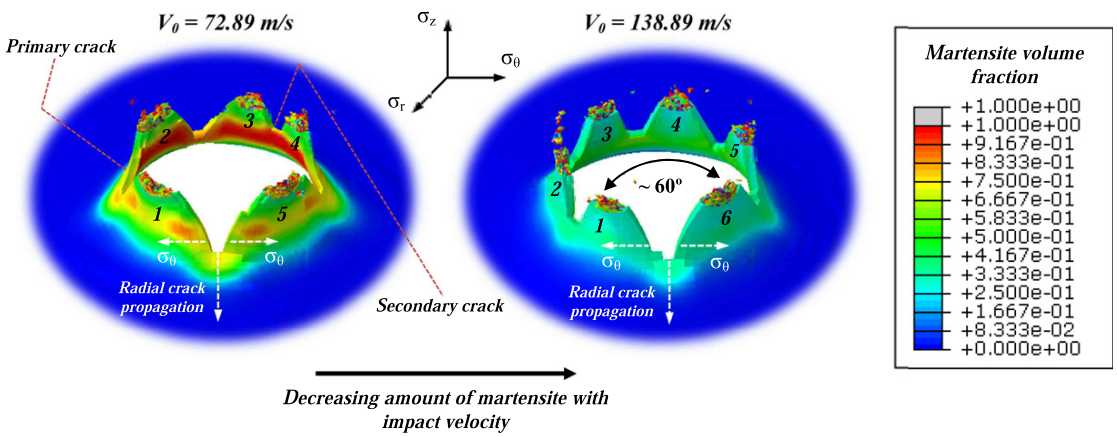

Fig. 14. Conical projectile configuration. Final stage of the perforation process for different impact velocities. Volume fraction of martensite contours. Target thickness $t_2 = 1.0$ mm.

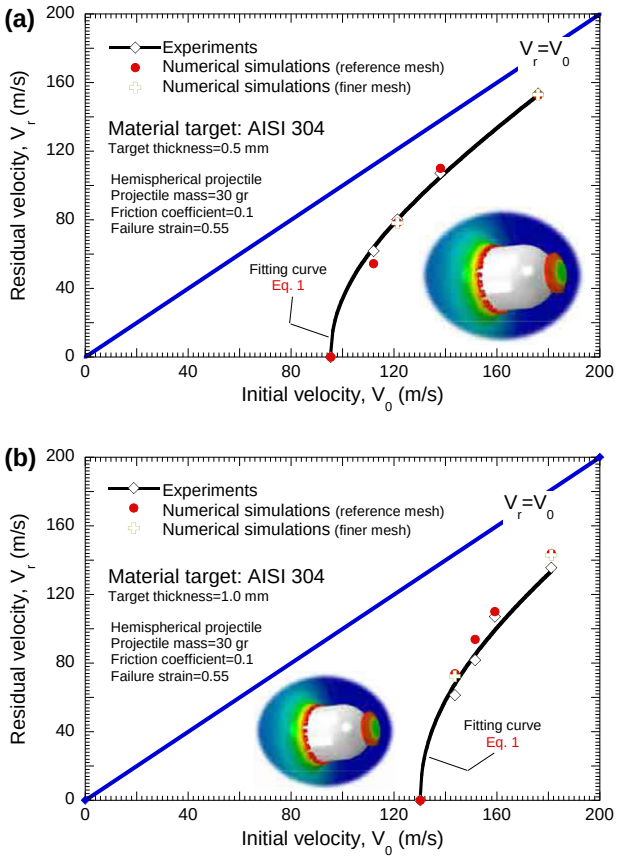

Fig. 15. Hemispherical projectile configuration. Residual velocity V_r versus initial velocity V_0. Comparison between experiments and numerical simulations. (a) Target thickness $t_1 = 0.5$ mm, (b) target thickness $t_2 = 1.0$ mm.

symmetries such as the radial expansion of ductile rings (Rusinek and Zaera, 2007).

Next, the γ to α' transformation predicted by the FE analysis is examined. The model predicts the formation of martensite within a narrow zone surrounding the impact location, as shown in Figs. 13 and 14. In particular, the SIMT process occurs in the cracking interfaces and the petals. This is in agreement with the experimental observations discussed above. There are two interesting findings:

- The amount of martensite decreases with the impact velocity, matching the experimental evidence reported in the literature, e.g., Rodríguez-Martínez et al. (2011a). At high strain rates, the material behaves under adiabatic conditions of deformation, and a temperature rise due to dissipation of plastic work occurs. The larger the initial velocity, the larger the strain rate level induced in the material due to the impact. The strain rate (due to positive material strain rate sensitivity) increases the flow stress of the material, and the rise in temperature becomes greater as the impact velocity increases. Therefore, at high impact velocities, the supply of free energy required to overcome the activation barrier between austenite and martensite must be greater (Angel, 1954; Olson and Cohen, 1975; Curtze et al., 2009). The slowdown of the SIMT process with increasing impact velocity is illustrated in Figs. 13 and 14. In the case of target thickness $t_1 = 0.5$ mm, shown in Fig. 13, the volume fraction of martensite observed in the petals after perforation at $V_0 = 54.53$ m/s varies within the range of 60–75%, while at $V_0 = 146.2$ m/s the fraction varies within the range of 25–45%. Similar observations can be made in the case of target thickness $t_2 = 1.0$ mm, shown in Fig. 14.
- The amount of martensite increases with target thickness, as can be observed in Figs. 13 and 14. The characteristic time of the perforation process increases, increasing the zone subjected to severe plastic deformation. This larger amount of energy in the form of plastic work transferred to the target material is used to overcome the energy barrier between austenite and martensite, enhancing the phase transformation.

Next, the FE results obtained for the hemispherical projectile configuration are presented.

7.2. Hemispherical projectile configuration

Fig. 15 shows the comparison between the experimental results and the numerical simulations in terms of V_r–V_0 curves for both target thicknesses examined. The numerical results obtained using both the reference mesh configuration (4 elements across the thickness) and a finer mesh (5 elements across the thickness) are shown. In both cases, the numerical results are practically identical, and the agreement with experiments is rather satisfactory, the difference being less than 10% over the entire range of impact velocities considered. The ballistic limit value is adequately captured. The mesh-independent numerical results allow the use of the reference mesh configuration with 4 elements across the thickness of the target in the hemispherical projectile simulations.

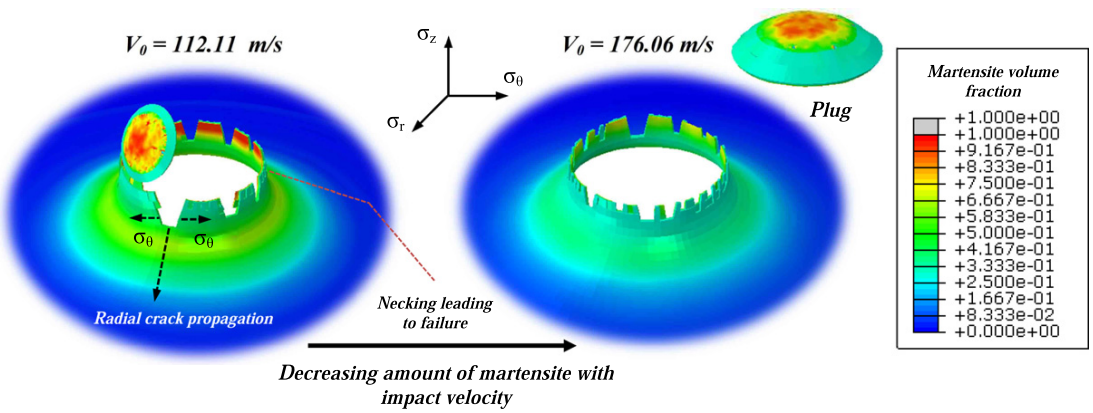

Fig. 16. Hemispherical projectile configuration. Final stage of the perforation process for different impact velocities. Volume fraction of martensite contours. Target thickness $t_1 = 0.5$ mm.

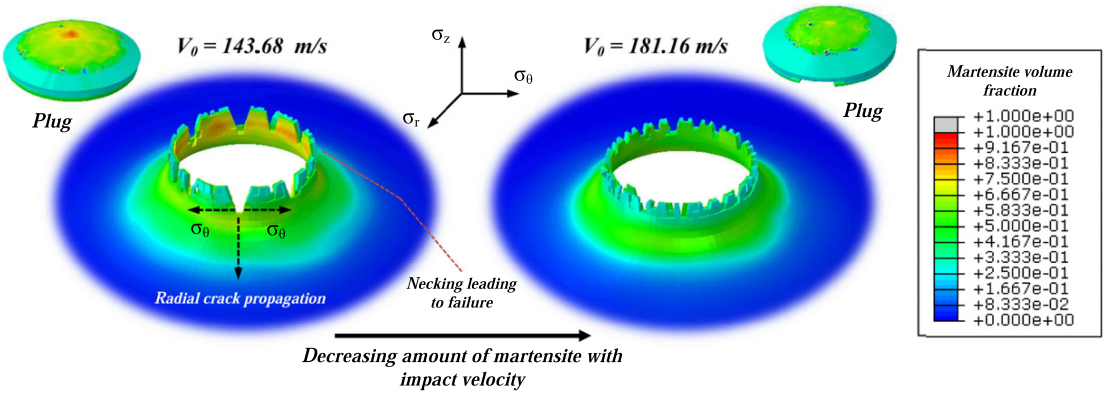

Fig. 17. Hemispherical projectile configuration. Final stage of the perforation process for different impact velocities. Volume fraction of martensite contours. Target thickness $t_2 = 1.0$ mm.

Furthermore, the model succeeds in defining the failure mechanisms associated with this projectile-target configuration. This reinforces the hypothesis concerning the applicability of the failure criterion (a constant value of plastic strain defining material failure) to capture the main aspects of the perforation process of thin steel sheets impacted by hemispherical and conical projectiles.

Necking and radial cracking around the perforations are observed for the entire range of impact velocities and both target thicknesses investigated, as shown in Figs. 16 and 17. During perforation, and enhanced by the effect of friction (Rusinek et al., 2009), the projectile coalesces with the steel sheet, leading to strain localization and failure. This leads to the formation of a plug as the final stage of the perforation process. At velocities close to the ballistic limit, the plug may not be completely ejected and the lack of symmetry in the failure mode predicted by the simulations may appear, as shown in Fig. 16. This non-symmetric failure mode is due to the numerical uncertainties associated with the mesh and the integration process when the impact velocity is sufficiently low. However, at high impact velocities, the ejection of the plug is complete and the failure mode is eminently symmetric. Moreover, the plug size depends on the impact velocity because it becomes smaller as the perforation speed decreases. Impact velocities close to the ballistic limit condition promote the radial sliding of the steel sheet along the projectile nose. Then, necking takes place close to the dome of the projectile/plate contact area, limiting the plug dimensions. In addition to the dependence of the necking location (and therefore the plug size) on the perforation speed, the FE model is also capable of describing qualitatively the interplay between the impact velocity and the radial cracking around the perforations. According to the experimental evidence reported in Section 4, the number of radial cracks formed increases with the impact velocity, as illustrated in Figs. 16 and 17.

It must be noted that the computational model predicts the formation of martensite during perforation over the entire range of

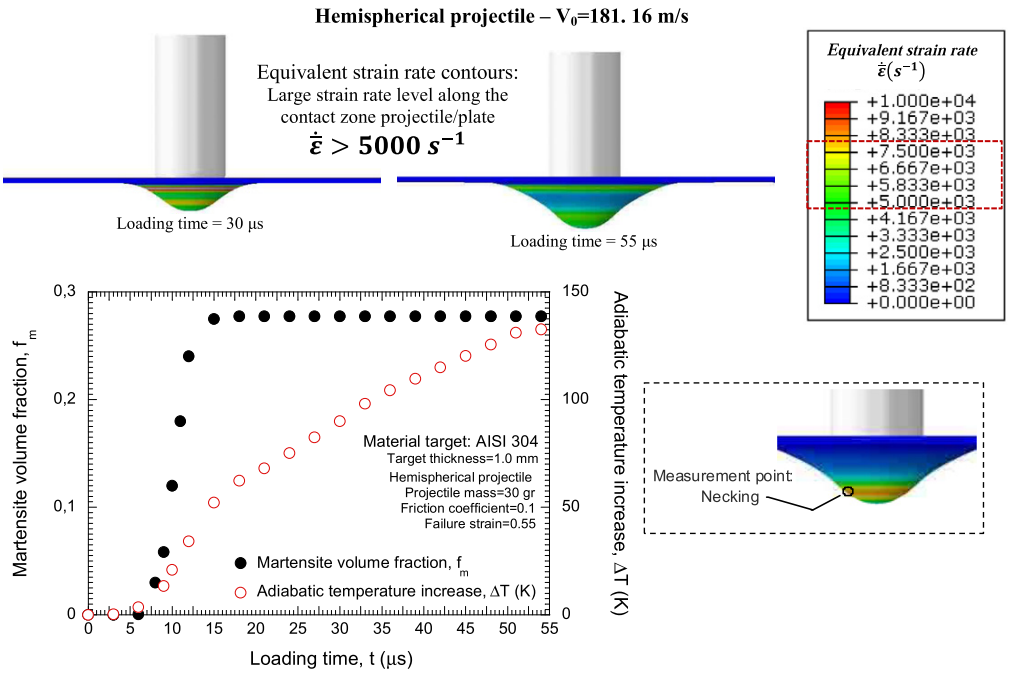

Fig. 18. Hemispherical projectile configuration. Homogenized strain rate contours for different stages of the perforation process. Martensite volume fraction and adiabatic temperature increase as a function of the loading time. Initial impact velocity $V_0 = 181.16$ m/s, target thickness $t_2 = 1.0$ mm.

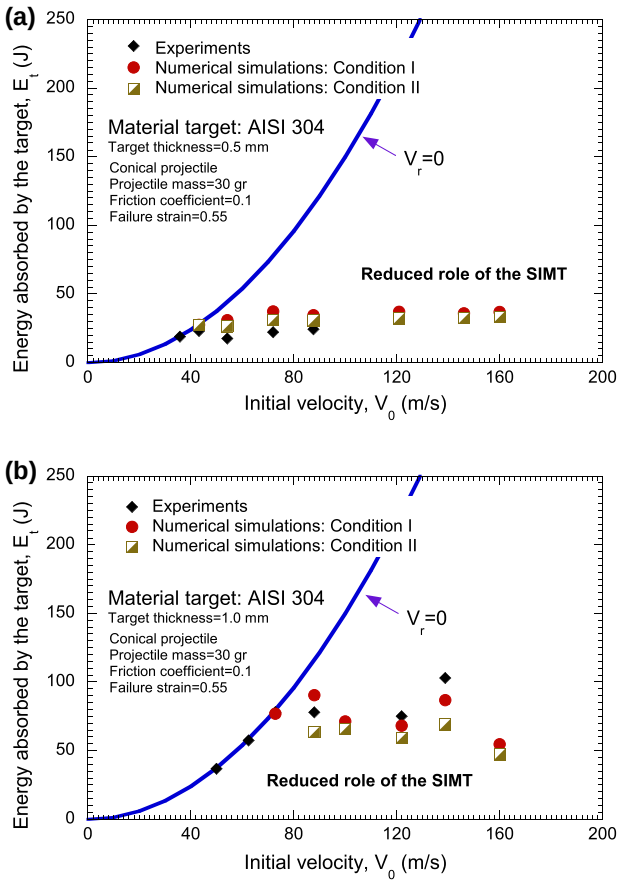

Fig. 19. Conical projectile configuration. Numerical predictions of the energy absorbed by the target E_t versus initial velocity V_0. (a) Target thickness $t_1 = 0.5$ mm, (b) target thickness $t_2 = 1.0$ mm.

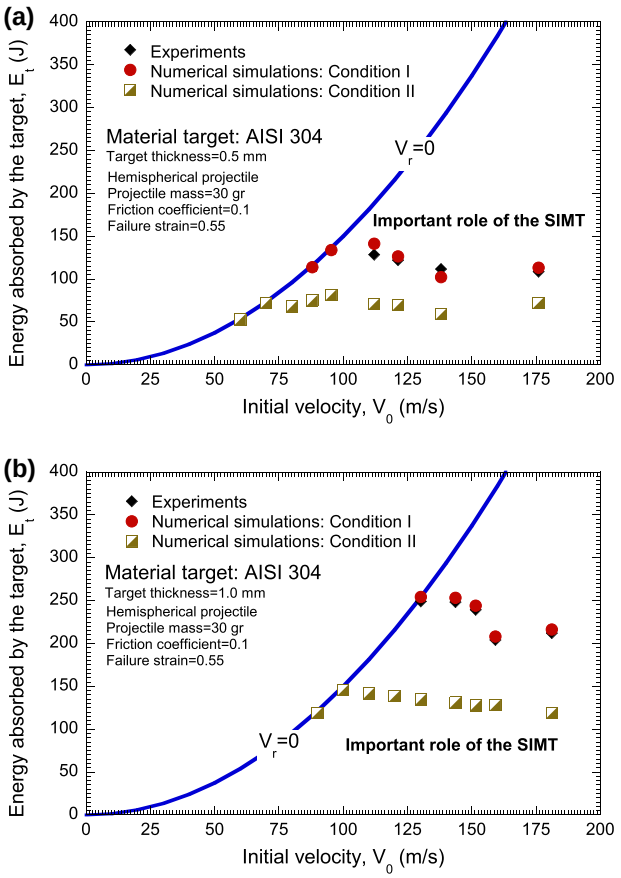

Fig. 20. Hemispherical projectile configuration. Numerical predictions of the energy absorbed by the target E_t versus initial velocity V_0. (a) Target thickness $t_1 = 0.5$ mm, (b) target thickness $t_2 = 1.0$ mm.

impact velocities examined for both target thicknesses considered. The SIMT process occurs in the cracking interfaces and the petals (as reported for the conical projectile configuration), but relevant quantities of martensite can also be detected within a wide area around the impact location, as can be observed in Figs. 16 and 17. The amount of martensite predicted in the FE analysis is greater for the hemispherical projectile configuration than for the conical one. This observation matches the experimental evidence described in Section 4.

Fig. 18 illustrates the time-dependent volume fraction of martensite developed in the necking for $V_0 = 181.164$ m/s and $t_2 = 1$ mm. The numerical model predicts the onset of the γ to α' transformation at the very beginning of the loading process. The target deformation rate during perforation reaches $\dot{\varepsilon} \approx 5000\ s^{-1}$ leading to a rapid increase in the temperature field. Thus, the volume fraction of martensite grows because of the target straining induced by the perforation until a certain limiting level of adiabatic temperature rise is reached, $\Delta T \approx 50$ K. From this point on, the temperature level exceeds the upper limit allowed for the SIMT and the volume fraction of martensite reaches saturation. This analysis provides the basis for a rational explanation of the γ to α' transformation observed in AISI 304 steel sheets subjected to high-rate loading processes. The threshold material straining required to overcome the activation barrier between austenite and martensite is lower than the material straining required to reach temperature limit that inhibits the transformation.

Finally, it has to be noted that the interplay between the impact velocity/target thickness and martensite formation determined for the conical projectile configuration is also predicted by the FE simulations run using the hemispherical configuration.

Next, further analysis of the role played by the SIMT in the perforation process is conducted.

7.3. The role played by the martensitic transformation in the perforation process

A number of FE simulations, in which the martensitic transformation was impeded were performed. This will be denoted as condition II. These numerical results are compared with those discussed in previous sections for which the SIMT was active. This will be denoted as condition I.

Fig. 19 shows, for the conical projectile configuration, the numerical predictions of the energy absorbed by the target E_t versus the impact velocity V_0 for conditions I and II and the comparison with the experimental results. It should be emphasized that, for any of the target thicknesses considered, the numerical results are practically independent of the condition applied, giving satisfactory agreement with the experimental evidence. The SIMT process plays a minor role in the ability of the target to absorb energy.

In comparison with the conical projectile configuration, a rather different behavior is detected for the hemispherical one, as shown in Fig. 20. Close to the ballistic limit, the energy absorbed by the steel sheet is significantly higher for condition I than for condition II. The results for condition I find good agreement with the experimental evidence. However if the SIMT is neglected, the difference between the numerical results and the experiments arises. The

material strain hardening plays a key role in the ability of the target to absorb energy. This reinforces the idea that, for the hemispherical projectile configuration, the SIMT process is a fundamental contributor to the process of energy absorption.

8. Conclusions and remarks

In this work, the mechanical behavior of AISI 304 metastable austenitic steel subjected to perforation was examined. Experimental tests were performed at several velocities, with conical and hemispherical projectiles, on AISI 304 sheet steels of two thicknesses. The tests were simulated with finite element models using a constitutive description that considers the thermoviscoplastic behavior and the phase transformation kinetics of the steel. The main conclusions that emerged from this work are as follows:

- Martensite was found in the specimens for the entire range of impact velocities, thus corroborating the ability of AISI 304 metastable austenitic steel to continue hardening because of a strain-induced martensitic transformation, even at high perforation rates.
- The extent of the region hardened by the martensite transformation and the amount of martensite transformed is clearly dependent on the deformation and the failure mode induced by the projectile. A sharp penetrator leads to radial cracks and to a small amount of stretching in the sheet, thus lessening SIMT, whereas a hemispherical penetrator leads to large membrane deformation before necking, thus promoting martensite nucleation.
- The amount of transformed martensite decreases with impact velocity because of the faster rise in temperature, which stabilizes austenite.
- The strain-induced martensitic transformation does not contribute to energy absorption in case of a sharp projectile. On the contrary, it substantially increases the dissipation of the kinetic energy through sheet deformation if the nose of the projectile is rounded.
- The finite element model succeeds in describing the perforation mechanisms associated with each projectile-target configuration analyzed. The roles played by the impact velocity, the target thickness and the projectile nose shape on the martensitic transformation are properly captured.
- The numerical model permits the observation that the characteristic time of the phase transformation process is shorter than that of the temperature increase. This explains the large amount of martensite found in the steel grade.

Acknowledgements

The researchers of the University Carlos III of Madrid are indebted to the Comunidad Autónoma de Madrid (Project CCG10-UC3M/DPI-5596) and to the Ministerio de Ciencia e Innovación de España (DPI2011–24068) for the financial support received which allowed conducting part of this work.

Professor A. Rusinek thanks M. Tavian, technician in LaBPS-ENIM, for his contribution to the development of the velocity sensors.

References

Andersson, R., 2005. Deformation characteristics of stainless steels. Ph.D. thesis, Lulea University of Technology, Sweden.

Angel, T., 1954. Formation of martensite in austenitic stainless steels. Effects of deformation, temperature and composition. Journal of Iron and Steel Institute 177, 165–174.

Arias, A., Rodríguez-Martínez, J.A., Rusinek, A., 2008. Numerical simulations of impact behaviour of thin steel to cylindrical, conical and hemispherical non-deformable projectiles. Engineering Fracture Mechanics 75, 1635–1656.

Atkins, A.G., Khan, M.A., Liu, J.H., 1998. Necking and radial cracking around perforations in thin sheets and normal incidence. International Journal of Impact Engineering 7, 521–539.

Backman, M., Goldsmith, W., 1978. The mechanics of penetration of projectiles into targets. International Journal of Engineering Sciences 16, 1–99.

Bao, Y., Wierzbicki, T., 2004. On fracture locus in the equivalent strain and stress triaxiality space. International Journal of Mechanical Sciences 46, 81–98.

Børvik, T., Langseth, M., Hopperstad, O., Malo, K.A., 2002a. Perforation of 12 mm thick steel plates by 20 mm diameter projectiles with flat, hemispherical and conical noses. Part I: Experimental study. International Journal of Impact Engineering 27, 19–35.

Børvik, T., Langseth, M., Hopperstad, O., Malo, K.A., 2002b. Perforation of 12 mm thick steel plates by 20 mm diameter projectiles with flat, hemispherical and conical noses. Part II: Numerical study. International Journal of Impact Engineering 27, 37–64.

Børvik, T., Langseth, M., Hopperstad, O.S., Malo, K.A., 1999. Ballistic penetration of steel plates. International Journal of Impact Engineering 22, 855–886.

Calder, C., Goldsmith, W., 1971. Plastic deformation and perforation of thin plates resulting from projectile impact. International Journal of Solids and Structures 7, 863–881.

Corbett, G., Reid, S., Johnson, W., 1996. Impact loading of plates and shells by free-flying projectiles: a review. International Journal of Impact Engineering 18, 141–230.

Corran, R., Shadbolt, P., Ruiz, C., 1983. Impact loading of plates – an experimental investigation. International Journal of Impact Engineering 1, 3–22.

Curtze, S., Kuokkala, V.T., Hokka, M., Peura, P., 2009. Deformation behavior of trip and dp steels in tension at different temperatures over a wide range of strain rates. Materials Science and Engineering A 507, 124–131.

Dan, W.J., Li, S.H., Zhang, W.G., Lin, Z.Q., 2008. The effect of strain-induced martensitic transformation on mechanical properties of trip steel. Materials and Design 29, 604–612.

De, A.K., Speer, J.G., Matlock, D.K., Murdock, D.C., Mataya, M.C., Comstock, R.J., 2006. Deformation-induced phase transformation and strain hardening in type 304 austenitic stainless steel. Metallurgical and Material Transactions A 37, 1875–1886.

Dean, J., Dunleavy, C., Brown, P., Clyne, T., 2009. Energy absorption during projectile perforation of thin steel plates and the kinetic energy of ejected fragments. International Journal of Impact Engineering 36, 1250–1258.

Dey, S., Brvik, T., Hopperstad, O.S., Leinum, J.R., Langseth, M., 2004. The effect of target strength on the perforation of steel plates using three different projectile nose shapes. International Journal of Impact Engineering 8–9, 1005–1038.

Glema, A., Lodygowski, T., Perzyna, P., 2000. Interaction of deformation waves and localization phenomena in inelastic solids. Computers Methods in Applied Mechanics and Engineering 183, 123–140.

Goldsmith, W., Finnegan, S., 1971. Penetration and perforation processes in metal targets at and above ballistic limits. International Journal of Mechanical Sciences 13, 843–866.

Gupta, N.K., Iqbal, M.A., Sekhon, G.S., 2006. Experimental and numerical studies on the behaviour of thin aluminium plates subjected to impact by blunt- and hemispherical-nosed projectiles. International Journal of Impact Engineering 32, 1921–1944.

Gupta, N.K., Iqbal, M.A., Sekhon, G.S., 2007. Effect of projectile nose shape, impact velocity and target thickness on deformation behaviour of aluminium plates. International Journal of Solids and Structures 44, 3411–3439.

Hecker, S.S., Stout, M.G., Staudhammer, K.P., Smith, J.L., 1982. Effects of strain and strain rate on deformation-induced transformation in 304 stainless steel: Part I. Magnetic measurements and mechanical behaviour. Metallurgical Transactions A 13A, 619–626.

HKS, 2010. Abaqus Explicit v6.10 User's Manual, version 6.10 Edition. Dassault Systèmes, 2010, Richmond, USA.

Huang, G.L., Matlock, D.K., Krauss, G., 1989. Martensite formation, strain rate sensitivity, and deformation behaviour of type 304 stainless steels sheet. Metallurgical Transactions 20A, 1239–1246.

Iwamoto, T., Tsuta, T., Tomita, Y., 1998. Investigation of deformation mode dependence of strain-induced martensitic transformation in trip steels and modelling of transformation kinetics. International Journal of Mechanical Sciences 40, 173–182.

Johnson, G.R., Cook, W.H., 1985. Fracture characteristics of three metals subjected to various strains, strain rates, temperatures and pressures. Engineering Fracture Mechanics 21, 31–48.

Jones, N., Paik, J., 2012. Impact perforation of aluminium alloy plates. International Journal of impact Engineering 48, 46–53.

Langdon, G.S., Schleyer, G.K., 2005a. Inelastic deformation and failure of profiled stainless steel blast wall panels. Part I: experimental investigations. International Journal of Impact Engineering 31, 341–369.

Langdon, G.S., Schleyer, G.K., 2005b. Inelastic deformation and failure of profiled stainless steel blast wall panels. Part II: Analytical modelling considerations. International Journal of Impact Engineering 31, 371–399.

Langdon, G.S., Schleyer, G.K., 2006. Deformation and failure of profiled stainless steel blast wall panels. Part III: Finite element simulations and overall summary. International Journal of Impact Engineering 32, 988–1012.

Lee, Y.W., Wierzbicki, T., 2005. Fracture prediction of thin plates under localized impulsive loading. Part II: Discing and petalling. International Journal of Impact Engineering 31, 1277–1308.

Leppin, S., Woodward, R., 1986. Perforation mechanisms in thin titanium alloy targets. International Journal of Impact Engineering 4, 107–115.
Lichtenfeld, J.A., Mataya, M., Tyne, C.J.V., 2006. Effect of strain rate on stress–strain behavior of alloy 309 and 304 l austenitic stainless steel. Metallurgical and Materials Transactions A 37A, 147–161.
Mertinger, V., Nagy, E., Tranta, F., Sólyom, J., 2008. Strain-induced martensitic transformation in textured austenitic stainless steels. Materials Science and Engineering A 481–482, 718–722.
Nemes, J.A., Eftis, J., 1993. Constitutive modelling on the dynamic fracture of smooth tensile bars. International Journal of Plasticity 9, 243–270.
Oliver, S., Jones, T.B., Foularis, G., 2007. Dual phase versus trip strip steels: microstructural changes as a consequence of quasi-static and dynamic tensile testing. Materials Characterization 58, 390–400.
Olson, G.B., Cohen, M., 1975. Kinetics of strain-induced martensitic nucleation. Metallurgical Transactions A 6A, 791–795.
Papatriantafillou, I., Aravas, N., Haidemenopoulos, G., 2004. Finite element modelling of trip steels. Steel Research International 75, 732–738.
Recht, R.F., Ipson, T.W., 1963. Ballistic perforation dynamics. Journal of Applied Mechanics 30, 384–390.
Rodríguez-Martínez, J.A., Pesci, R., Rusinek, A., 2011a. Experimental study on the martensitic transformation in AISI 304 steel sheets subjected to tension under wide ranges of strain rate at room temperature. Materials Science and Engineering A 528, 5974–5982.
Rodríguez-Martínez, J.A., Pesci, R., Rusinek, A., Arias, A., Zaera, R., Pedroche, D.A., 2010a. Thermo-mechanical behaviour of TRIP 1000 steel sheets subjected to low velocity perforation by conical projectiles at different temperatures. International Journal of Solids and Structures 47, 1268–1284.
Rodríguez-Martínez, J.A., Rusinek, A., Arias, A., 2011b. Thermo-viscoplastic behaviour of 2024-t3 aluminium sheets subjected to low velocity perforation at different temperatures. Thin-Walled Structures 49, 819–832.
Rodríguez-Martínez, J.A., Rusinek, A., Chevrier, P., Bernier, R., Arias, A., 2010b. Temperature measurements on ES steel sheets subjected to perforation by hemispherical projectiles. International Journal of Impact Engineering 37, 828–841.
Rodríguez-Martínez, J.A., Rusinek, A., Pesci, R., 2010c. Experimental survey on the behaviour of AISI 304 steel sheets subjected to perforation. Thin-Walled Structures 48, 966–978.
Rusinek, A., Rodríguez-Martínez, J.A., Zaera, R., Klepaczko, J.R., Arias, A., Sauvelet, C., 2009. Experimental and numerical study on the perforation process of mild steel sheets subjected to perpendicular impact by hemispherical projectiles. International Journal of Impact Engineering 36, 565–587.
Rusinek, A., Zaera, R., 2007. Finite element simulation of steel ring fragmentation under radial expansion. International Journal of Impact Engineering 34, 799–822.
Stringfellow, R.G., Parks, D.M., Olson, G.B., 1992. A constitutive model for transformation plasticity accompanying strain-induced martensitic transformations in metastable austenitic steels. Acta Metallurgica et Materialia 40 (7), 1703–1716.
Suquet, P., 1995a. Overall properties of nonlinear composites: a modified secant moduli theory and its link to Ponte Castañeda's nonlinear variational procedure. Comptes Rendus de L Academie des Sciences, Sèrie IIb 320, 563–571.
Suquet, P., 1995b. Overall properties of nonlinear composites: Secant moduli theories and variational bounds. In: Markov, K.Z. (Ed.), Continuum Models and Discrtete Systems, Proceedings of 8th International Symposium. World Scientific Publishing Company, pp. 290–299.
Suquet, P., 1996. Overall properties of nonlinear composites: remarks on secant and incremental formulations. In: Pineau, Pineau, Zaoui, A. (Eds.), Micromechanics of Plasticity and Damage of Multiphase Materials (IUTAM Symposium). Kluwer, pp. 149–156.
Teng, X., Wierzbicki, T., 2006. Evaluation of six fracture models in high velocity perforation. Engineering Fracture Mechanics 73, 1653–1678.
Tomita, Y., Iwamoto, T., 1995. Constitutive modelling of trip steel and its application to the improvement of mechanical properties. International Journal of Mechanical Sciences 37, 1295–1305.
Tomita, Y., Iwamoto, T., 2001. Computational prediction of deformation behavior of trip steels under cyclic loading. International Journal of Mechanical Sciences 43, 2017–2034.
Voyiadjis, G.Z., Abed, F.H., 2006. A coupled temperature and strain rate dependent yield function for dynamic deformations of bcc metals. International Journal of Plasticity 22, 1398–1431.
Wierzbicki, T., 1999. Petalling of plates under explosive and impact loading. International Journal of Impact Engineering 22, 935–954.
Wood, W.W., 1965. Experimental mechanics at velocity extremes very high strain rates. Experimental Mechanics 5, 361–371.
Zaera, R., Rodríguez-Martínez, J.A., Casado, A., Fernández-Sáez, J., Rusinek, A., Pesci, R., 2012. A constitutive model for analyzing martensite formation in austenitic steels deforming at high strain rates. International Journal of Plasticity 29, 77–101.
Zhang, H., Ravi-Chandar, K., 2008. On the dynamics of necking and fragmentation – II. Effect of material properties geometrical constraints and absolute size. International Journal of Fracture 150, 3–36.